Chemical Geology 268 (2009) 167–179

Contents lists available at ScienceDirect

Chemical Geology

journal homepage: www.elsevier.com/locate/chemgeo

High-precision determination of iron oxidation state in silicate glasses using XANES

Elizabeth Cottrell [a,*], Katherine A. Kelley [b], Antonio Lanzirotti [c], Rebecca A. Fischer [a]

[a] Smithsonian Institution, National Museum of Natural History, Washington, DC 20560, USA
[b] Graduate School of Oceanography, University of Rhode Island, Narragansett, RI 02882, USA
[c] University of Chicago, Center for Advanced Radiation Sources, Chicago, IL 60637, USA

ARTICLE INFO

Article history:
Received 23 December 2008
Received in revised form 1 June 2009
Accepted 13 August 2009

Editor: D.B. Dingwell

Keywords:
XANES
Oxidation state
Iron
Mossbauer spectroscopy
Silicate melt
Silicate glass

ABSTRACT

Fe K-edge X-ray absorption near-edge structure (XANES) and Mössbauer spectra were collected on natural basaltic glasses equilibrated over a range of oxygen fugacity (QFM −3.5 to QFM +4.5). The basalt compositions and fO_2 conditions were chosen to bracket the natural range of redox conditions expected for basalts from mid-ocean ridge, ocean island, back-arc basin, and arc settings, in order to develop a high-precision calibration for the determination of $Fe^{3+}/\sum Fe$ in natural basalts. The pre-edge centroid energy, corresponding to the 1s→3d transition, was determined to be the most robust proxy for Fe oxidation state, affording significant advantages compared to the use of other spectral features. A second-order polynomial models the correlation between the centroid and $Fe^{3+}/\sum Fe$, yielding a precision of ±0.0045 in $Fe^{3+}/\sum Fe$ for glasses with $Fe^{3+}/\sum Fe > 8\%$, which is comparable to the precision of wet chemistry. This high precision relies on a Si (311) monochromator to better define the Fe^{2+} and Fe^{3+} transitions, accurate and robust modeling of the pre-edge feature, dense fO_2-coverage and compositional appropriateness of reference glasses, and application of a non-linear drift correction. Through re-analysis of the reference glasses across three synchrotron beam sessions, we show that the quoted precision can be achieved (i.e., analyses are reproducible) across multiple synchrotron beam sessions, even when spectral collection conditions (detector parameters or sample geometry) change. Rhyolitic glasses were also analyzed and yield a higher centroid energy at a given $Fe^{3+}/\sum Fe$ than basalts, implying that major variations in melt structure affect the relationship between centroid position and $Fe^{3+}/\sum Fe$, and that separate calibrations are needed for the determination of oxidation state in basalts and rhyolites.

Published by Elsevier B.V.

1. Introduction

The oxygen fugacity of earth's interior is intimately linked to mineral assemblage, element partitioning, magmatic differentiation, and volcanic degassing. The ratio of oxidized to reduced iron (i.e., $Fe^{3+}/\sum Fe = Fe^{3+}/[Fe^{3+} + Fe^{2+}]$) in mantle-derived basaltic melts is a proxy for mantle oxygen fugacity (fO_2), revealing current oxidation conditions in the earth's interior (e.g., Arculus, 1985; Christie et al., 1986; Wood et al., 1990; Kress and Carmichael, 1991; Lecuyer and Ricard, 1999; Bezos and Humler, 2005). Bulk techniques (e.g., wet chemistry, colorimetry, Mössbauer spectroscopy) are often incapable of capturing the $Fe^{3+}/\sum Fe$ of natural, true magmatic liquids due to the presence of crystals. Moreover, bulk techniques preclude the determination of $Fe^{3+}/\sum Fe$ at the same micro-scales as other analytical methods well-suited to the characterization of natural glasses for elemental concentrations (EMP, SIMS, LA-ICP-MS), volatile concentrations (FTIR, SIMS), and isotopic ratios (LA-ICP-MS, SIMS, SHRIMP). Here we present a high-precision micro X-ray absorption near-edge structure (μ-XANES) calibration for natural basalt compositions, for application to the direct, *in situ* microanalysis of $Fe^{3+}/\sum Fe$ in primitive, undegassed, natural magmatic liquids (i.e., homogeneous, crystal-free glass) at the small scales needed to sample such liquids in natural systems (e.g., pillow glasses and melt inclusions).

XANES is sensitive to element valence state, which, for certain elements, changes in response to the oxygen fugacity of a system. In the case of Fe, the pre-edge feature, occurring approximately 10 eV before the main K-edge absorption, is particularly sensitive to valence state and is related to the 1s→3d electronic transition (Calas and Petiau, 1983; Waychunas et al., 1983; Drager et al., 1988; Bajt et al., 1994). The centroid, or area-weighted average energy of the pre-edge peaks, shifts to higher energy as the ratio of ferric to ferrous iron increases, allowing quantification of $Fe^{3+}/\sum Fe$ in minerals and glasses provided an empirical calibration is available for reference materials of known oxidation state (Bajt et al., 1994; Delaney et al., 1998; Dyar et al., 1998; Dyar et al., 2001; Wilke et al., 2001; Berry et al., 2003a; McCanta et al., 2004; Wilke et al., 2005). Quantitative precision improves when the calibration materials are structurally similar to the unknowns because the pre-edge feature is sensitive to coordination geometry as well as valence state. Precise determination of the oxidation state of Fe in glasses, where the coordination

* Corresponding author.
E-mail address: cottrellE@si.edu (E. Cottrell).

0009-2541/$ – see front matter. Published by Elsevier B.V.
doi:10.1016/j.chemgeo.2009.08.008

geometry is poorly constrained, therefore benefits from a glass-based calibration when compared to linear combinations of crystalline end-member oxides (e.g. Berry et al., 2003a; Botcharnikov et al., 2005; Wilke et al., 2005).

μ-XANES affords many advantages to bulk techniques (e.g., wet-chemistry and Mössbauer spectroscopy) because of its small spatial resolution ($<10\times10$ μm), allowing the oxidation state to be determined on the same spatial scale as other microbeam analytical techniques (LA-ICP-MS, EMP, FTIR, SIMS). Several studies have already taken advantage of this high spatial precision to investigate the $Fe^{3+}/\sum Fe$ of melt inclusions (Bonnin-Mosbah et al., 2001; Metrich et al., 2006; Berry et al., 2008; Kelley and Cottrell, 2009) and to explore Fe oxidation state *in situ* under controlled conditions (e.g. Waychunas et al., 1988; Jackson et al., 1993; Berry et al., 2003b; Metrich et al., 2006; Kavner et al., 2007). These pioneering studies demonstrate the potential of XANES to extract redox information from silicate glasses and provide an impetus for the development of a high-precision, composition-specific calibration and a methodology to ensure session-to-session measurement reproducibility at synchrotron radiation sources.

Here we present a μ-XANES basaltic glass calibration specifically developed for application to basaltic glasses and melt inclusions from mid-ocean ridge (MORB), oceanic island, back-arc basin (BABB), and arc settings. In this study, we analyze the same series of 16 basaltic reference glasses a minimum of three times per synchrotron session and across three distinct sessions (>144 spectra) to rigorously evaluate the methods by which Fe oxidation state can be determined and the factors that control measurement reproducibility. From this vantage point, we present a methodology by which XANES can be used to extract $Fe^{3+}/\sum Fe$ with the precision of wet-chemical analyses. The composition of the reference glass suite was chosen specifically for the analysis of basalts, but we also present analyses of a rhyolitic glass suite to examine the effect of composition on the relationship between centroid energy and $Fe^{3+}/\sum Fe$. Our data indicate that this relationship is insensitive to small variations in basalt major element composition. In contrast with previous work, however, large compositional variations (e.g., between rhyolites and basalts) appear to require independent calibration of $Fe^{3+}/\sum Fe$ as a function of centroid energy. We address several issues related to the utility of μ-XANES in quantifying $Fe^{3+}/\sum Fe$ from natural basaltic glasses, such as (1) factors controlling session-to-session reproducibility (precision) and (2) the effect of composition on the relationship between the centroid position and $Fe^{3+}/\sum Fe$.

2. Experimental methods

2.1. Starting materials

Four starting materials are examined in this study: two natural basalt compositions and two rhyolites (Table 1). A series of 1 atm gas-mixing experiments were carried out on two metaluminous basalt powders from whole rock samples of Mid-Atlantic Ridge MORB, AII-92-29-1 (Smithsonian catalog number: 113707-2, volcanic glass collection number: VG2524; Shimizu et al., 1980), and a Hawaiite from lava flow LW-QL2a, erupted from the Lathrop Wells volcanic center in the Crater Flat volcanic zone, Nevada (Nichols and Rutherford, 2004). These two compositions bracket the range of major element compositions expected for basalts from MORB and arc settings. To investigate the versatility of our calibration curve, we also equilibrated chips of metaluminous rhyolite glass from Obsidian Cliffs, Yellowstone National Park (Smithsonian volcanic glass collection number: VG568, SI catalog number: 72854) and analyzed several of the synthetic peralkaline rhyolitic glasses (NZC-4) from the study of Moore et al. (1995).

2.2. High temperature experiments

Basaltic glasses were equilibrated at 1 atm in a vertical gas-mixing rapid-quench furnace from QFM −3.5 to QFM +4.5, to encompass the range of oxygen fugacities expected in natural settings. The hot-spot was mapped following the procedure of Walker et al. (1988) and the temperature was calibrated relative to the melting point of gold before and after the experimental series and is considered accurate to ±2 °C. Pt loops (0.2 mm diameter) were pre-equilibrated with the starting material by loading approximately 150 mg of basalt powder, bonded by PVA, on the loops and holding them at the experimental temperature and fO_2. The loops were then cleaned in HF and reloaded with starting material. Electron microprobe analyses on each glass verified that this procedure prevented any Fe loss from taking place during the experiment. The high viscosity of the rhyolite, however, precluded the use of PVA. The resulting glass from PVA-bonded rhyolites had bubbles remaining, even after 48–72 h, and XANES analyses revealed ubiquitous micro-scale fO_2 heterogeneity and $Fe^{3+}/\sum Fe$ increasing from the bead edge to interior bubble interfaces. Similar heterogeneity, even on the scale of wet-chemical analysis, was reported by Moore et al. (1995) after using PVA. We therefore adopted the procedure of Moore et al. (1995) and pre-equilibrated and performed experiments on natural solid chips of rhyolitic glass tied to the Pt.

The basalts were equilibrated at 1350 °C in CO/CO_2 for 24 h (except glass AII_+4.5, which was equilibrated in CO_2/O_2). This length of time was sufficient to completely equilibrate Fe speciation in this system (Kilinc et al., 1983; Roskoz et al., 2008). The rhyolite VG568 chip was held at 1550 °C for 72 h following Moore et al. (1995). All glasses were rapidly drop quenched into a water bath by vaporizing the Pt hang wire, and then carefully separated from the Pt loops. Several chips were removed from each glass and double-side polished for optical examination, XANES, and electron microprobe analyses, while the remainder was ground to a powder for Mössbauer spectroscopy. Polished sections (~100 μm thick) were examined optically and with Smithsonian's field emission FEI NOVA nanoSEM600 FEG Variable Pressure Scanning Electron Microscope. Basalt samples varied systematically in color as a function of oxidation state from dark brown (most oxidized) to very pale yellow (most reduced) and appeared glassy and crystal-free down to the scale of several hundred nanometers. All NZC-4

Table 1
Chemical composition of reference glasses in oxide weight percent.

	LW[a]	AII[b]	VG568[c]	NZC-4[d]				
				DT_46	DT_39	H2O_63	DT_31	DT_18
SiO_2	49.42 (0.69)	50.81 (0.60)	77.51 (0.63)	74.40	73.10	70.40	77.30	72.60
TiO_2	1.94 (0.07)	1.73 (0.02)	0.07 (0.02)	0.25	0.26	0.23	0.25	0.25
Al_2O_3	17.21 (0.49)	16.14 (0.11)	12.52 (0.93)	10.10	9.90	9.50	10.50	9.90
FeO^{TOT}	10.17 (0.50)	9.53 (0.60)	1.31 (0.13)	–	–	–	–	–
Fe_2O_3	–	–	–	3.58	1.99	3.46	3.01	3.89
FeO	–	–	–	2.44	3.89	2.11	1.59	1.80
MgO	6.13 (0.19)	7.40 (0.06)	0.03 (0.01)	0.01	0.01	0.02	0.03	0.01
CaO	8.78 (0.07)	11.20 (0.12)	0.5 (0.05)	0.24	0.24	0.24	0.23	0.19
Na_2O	3.17 (0.02)	2.75 (0.19)	3.11 (0.15)	4.57	5.01	5.22	3.29	4.76
K_2O	1.50 (0.04)	0.15 (0.01)	4.57 (0.12)	4.48	4.36	4.26	3.33	4.31
P_2O_5	1.12 (0.19)	0.14 (0.02)	<0.01	–	–	–	–	–
Total	99.35 (0.61)	100.05 (0.51)	99.65 (0.72)	100.10	98.72	95.44	99.56	97.81

[a] Nicols and Rutherford, Hawaiite LW.QL-2. 1σ for analyses of six experimental reference glasses, 6 analyses per glass ($n=36$).
[b] Shimizu et al. (1980). MORB AII-92-29-1. 1σ for analyses of 10 experimental reference glasses, 6 analyses per glass ($n=60$).
[c] Jarosewich et al. (1980). 1σ for analyses of 1 experimental reference glass (VG568_2), $n=9$.
[d] Wet-chemical and probe analysis from Moore et al. (1995).

rhyolitic glasses were equilibrated as described by Moore et al. (1995). Most samples only had a few milligrams of material remaining, but DT-39 and DT-46 had enough material for Mössbauer analysis.

3. Analytical methods

3.1. Mössbauer spectroscopy

$Fe^{3+}/\sum Fe$ ratios were independently determined on the experimental reference glasses using Mössbauer spectroscopy in collaboration with Bjorn Mysen at the Geophysical Laboratory, Carnegie Institution of Washington. Approximately 100 mg of sample were ground to powder in agate, mixed in a 1:1 ratio by weight with cellulose, and pressed into 10 mm diameter pellets (approximate absorber thickness equal to 12–13 mg Fe/cm^2). ^{57}Fe spectra were collected at room temperature in constant acceleration transmission mode on a nominal 50mCi ^{57}Co source. The Mössbauer drive was calibrated with Fe foil. Spectra were collected for 1–2 days, corresponding to approximately 8×10^6 counts per channel and were fit using the algorithm of Alberto et al. (1996), which adopts a two-dimensional Gaussian probability distribution function for the isomer shift and quadrupole splitting. $Fe^{3+}/\Sigma Fe$ was calculated from the ratio of the area of the fitted Fe^{3+} doublet relative to the entire resonant absorption envelope with no correction for recoil-free fractions. Reliance on 298 K spectra for this purpose has found support in comparative analytical studies; for example, Mysen et al. (1985b) and Dingwell (1991) performed Mössbauer and wet-chemical analyses on the same samples and found no systematic difference in the redox ratio. Mössbauer spectroscopic studies of glasses at both ambient and cryonic temperatures reveal no temperature effects within the reported 2–4% relative uncertainty in redox ratio (e.g., Jayasuriya et al., 2004; Mysen and Richet, 2005; Mysen and Shang, 2005).

3.2. Xanes

3.2.1. Spectral collection

Fe K-edge XANES spectra were collected at station X26A (bending magnet) at the National Synchrotron Light Source (NSLS), Brookhaven National Lab (BNL), in four synchrotron sessions (three sessions for basalts and one for rhyolites) such that a minimum of 9 spectra were collected on each of the basaltic reference glasses and 3 on each of the rhyolites. NSLS operates at 2.8 GeV and 300 mA. The spot size on the sample was 9x5 μm. Energy selection was achieved with silicon channel-cut monochromators, and we tested both Si (311) and Si (111) lattice cuts. The improvement in spectral resolution afforded by a Si (311) relative to a (111) crystal (d-spacing of 1.64 vs. 3.14 Å) can be seen in Fig. 1, and its impact on the overall precision with which oxidation state can be determined will be considered in Section 4.2.2. The specifications provided below apply to the Si (311) monochromator and all data presented in this study were collected using the Si (311).

The crystal holder/translation assembly was mounted to a Huber 410 rotational stage with 20:1 gear reducer that provides rotator resolution of about 5×10^{-5} degrees. The first derivative peak for Fe foil, set to 7112 eV, defines the energy calibration for the system. Monochromators were water cooled to 9 °C. Considering current NSLS source size parameters and collimation of the source to 0.2 mm using beamline white beam slits, the X26A Si (311) monochromator should provide an overall spectral resolution of about 1.04 eV, reflecting a 0.36 eV Darwin width for Si (311) and 0.98 eV broadening from the source divergence (calculated using ALINE, Berman, 1981).

The inherent nature of the natural glasses targeted in our application necessitates that XANES spectra be collected in fluorescence mode, rather than transmission. Volcanic glasses have relatively dilute and variable atomic concentrations of iron (~1 at.% Fe in rhyolites to ~10 at.% Fe in basalts) and are necessarily of variable thickness. For example, glass inclusions in minerals and crystal-rich basalts may require a thin (~30–40 μm) preparation to fully expose a clear path through the glass without any interference from crystals, whereas very glassy pillow basalt may be prepared at a greater thickness (~400 μm) to facilitate FTIR analysis of low-abundance volatile elements. Moreover, the small spatial scales and chemical heterogeneity inherent in these samples necessitate the use of micro-focused spectroscopy and fluorescence analysis. Collection in fluorescence mode allows direct comparison of Fe oxidation states between these

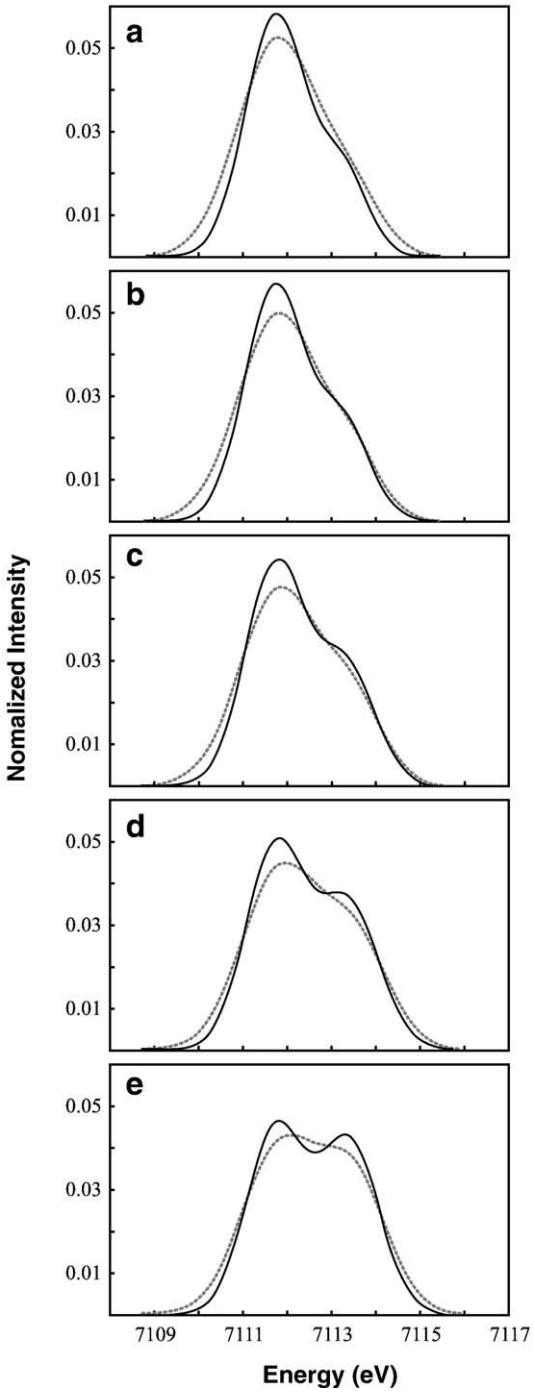

Fig. 1. Comparison of baseline-subtracted μ-XANES pre-edge spectra collected using Si-111 (dashed curves) and −311 (solid curves) monochromators for five experimental reference glasses equilibrated over a range of oxygen fugacities. Reference glasses shown are (a) LW_−20 (QFM −2), (b) LW_−10 (QFM −1), (c) LW_0 (QFM), (d) LW_10 (QFM +1), and (e) LW_20 (QFM +2).

diverse samples and preparations; however, glasses with high Fe contents then require appropriate evaluation of self-absorption and detector pulse-pileup effects (Section 4.2.3).

Fluorescence was measured with 9 and 13 element Ge array detectors (Canberra) utilizing digital spectrometers (XIA). Across the four beam sessions presented in this study, detector shaping times between 0.8 and 6 μs were used. In some instances aluminum filters were used to reduce high count-rates above the Fe K absorption edge and to keep detector dead times below 25%. Spectra were recorded from 7020 to 7220 eV with four regions: 10 eV steps from 7020 to 7105 eV with 1 s dwell, 0.1 eV steps over the pre-edge from 7106 to 7118 eV at 5 s dwell, 1.0 eV steps from 7118 to 7140 eV with a 2 s dwell, and 4.0 eV steps from 7141 to 7220 eV at 2 s dwell. Decreasing the step size over the pre-edge did not improve the standard deviations of the area-weighted centroid positions. This guided the choice of step size across the spectrum, optimizing the precision with which oxidation state can be determined while minimizing the overall analysis time. Spectra were normalized to the incident photon flux measured using an ion chamber upstream of the sample.

A minimum of three spectra were recorded on each calibration glass, each on a unique spot, at each beam session. Sessions lasted from 3 to 5 days, and we returned to the calibration glasses over the course of a beam session, and from session to session, for a total of 144 analyses on 16 samples, to assess the reproducibility of the pre-edge position. Acquiring multiple spectra on each glass across time and space allows quantitative assessment of reproducibility and precision.

3.2.2. Spectral fitting of the pre-edge

Spectra were normalized for atomic absorption by the average absorption coefficient of the edge-step region from 7200 to 7220 eV to account for differences in the mass of the absorber between analysis points. For the range of Fe oxidation states in these glasses and the resulting coordination geometries, the pre-edge spectra are best defined by two multiple 3d crystal field transitions. The pre-edge feature is difficult to deconvolve from the absorption baseline of the main Fe absorption edge and is hence highly sensitive to the baseline subtraction and peak fitting routine (Berry et al., 2003a; Farges et al., 2004). Different fitting models and functions result in small but significant differences in the calculated peak area of each pre-edge multiplet and the relative contribution of each peak to the calculated centroid. As Berry et al. (2003a) note, the choice of function is less significant than its consistent application to standards and unknowns. We find, however, that the choice of function affects the consistency and reproducibility of the spectral fits. Centroid positions in this study were extracted by simultaneously fitting the baseline with a linear function constrained to have a positive slope and a damped harmonic oscillator (DHO) function, and the pre-edge peaks with two Gaussian functions over a 7110–7118 eV sub-sample of the pre-edge region containing 80 channels using Interactive Data Language (IDL) software and the MPFIT set of routines for robust least-squares minimization (Markwardt, 2008). Increasing the window over which the pre-edge was extracted did not result in more precise modeling of the pre-edge feature, whereas fitting a narrower window did degrade the precision of the fits for the most oxidized samples ($Fe^{3+}/\sum Fe > 0.6$). Fixing the centers of the Gaussians and fitting the components individually both resulted in significantly poorer fits.

The DHO function yielded a superior fit relative to spline, Lorentzian, and pseudo-Voigt functions, all of which yielded residuals with greater amplitude and more structure (greater misfit) on either side of the pre-edge peaks. Application of the DHO function to the baseline resulted in approximately a factor of two improvement in the reproducibility of the fits relative to spline, Lorentzian, and pseudo-Voigt functions. Farges et al. (2004) provide a detailed discussion on the importance of the chosen function to robust modeling of the pre-edge and emphasized the use of pseudo-Voigt functions to fit the pre-edge feature of crystalline compounds. We find, however, that fitting the pre-edge features of our glasses with pseudo-Voigt functions or pure Lorentzians resulted in a residual misfit at energies just above and below the pre-edge feature, whereas extremely precise fits could be obtained with pure Gaussians, which have fewer free parameters than pseudo-Voigt functions. This approach yielded fits that were nearly perfectly reproducible across the range of pre-edge shapes recorded. A typical spectrum, pre-edge, component fits, and residual is shown in Fig. 2 for basalt glass AII_0, which falls mid-way along our calibration with 14.7% ferric iron, and for rhyolitic glass DT_18 (Figure A1).

3.2.3. Drift correction

Drift in monochromator energy with time at X26A, primarily related to changes in thermal load on the monochromator crystal as a function of storage ring current, is significant (~0.2 eV over 12 h) relative to the natural variations that we aim to resolve (±0.01 eV). Energy reproducibility and instrumental drift were therefore monitored continuously throughout each experimental session using a reference glass (LW_0) as an energy drift monitor. Spectra on the drift monitor LW_0 were recorded alternately between each sample (every ~16 min) for the first 2–2.5 h after beam reinjection (nominally every

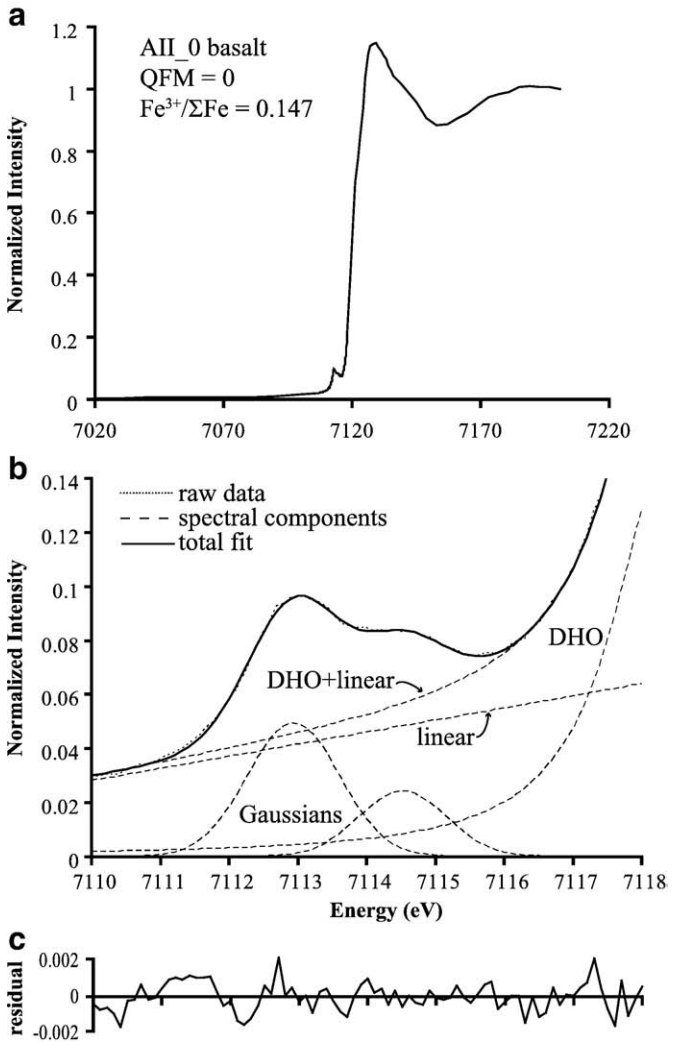

Fig. 2. XANES spectrum of basaltic glass AII_0 with $Fe^{3+}/\sum Fe * 100 = 14.7$. (a) Edge-step normalized data (not referenced to drift monitor LW_0 = 7112.3) of the full XANES spectrum and (b) magnified view of the pre-edge feature (dotted line). The four components of the model fit (linear, DHO, and two Gaussians) are shown as dashed lines and the summation of those components, creating the overall fit to the spectrum, is shown as a solid black line. (c) The residual misfit as a function of energy when the model fit is subtracted from the raw spectrum. The quality of the fit of this glass is representative of all fits in this study.

12 h at X26A), when the silicon thermal response varies non-linearly. After 2–2.5 h, when the beam current is in approximately linear decay, spectra of LW_0 were recorded every 5 samples (Fig. 3). We define the centroid energy of sample LW_0 ≡ 7112.3, and model the energy drift as a linear function between each analysis of LW_0. Closer spacing of the drift monitor analyses, as in the early hours of each fill cycle, allows for more accurate correction of non-linear energy drift. This drift correction routine is exactly analogous to non-linear drift corrections often applied for solution-based ICP-MS analyses (e.g., Cheatham et al., 1993). Its application yields an average reproducibility for the basalt reference glasses that is indistinguishable within error from the expected spectral resolution of the Si (311) monochromator at this beamline. This is based on replicate analyses separated in time and space within a single beam session and across beam sessions even when collection conditions change (shaping time, filters, detectors, etc.; see Sections 4.2.2, 4.2.3, and Table 2).

Use of a drift monitor permits direct comparison of centroids and $Fe^{3+}/\sum Fe$ between beam sessions, and potentially even between synchrotron facilities. This is a key advantage because, even on a single beam line, modifications are often made over time to operational hardware and software that make it impossible to acquire data under exactly the same conditions at each visit.

3.3 Electron microprobe

Electron microprobe analyses of experimental reference glasses were performed on Smithsonian's JEOL-8900 5 spectrometer microprobe. Major and minor elements (Table 1) were analyzed at 15 kV accelerating potential with a defocused (10–20 μm) beam and 10 nA beam current. Glasses were analyzed in ~6 spots for SiO_2, TiO_2, Al_2O_3, FeO^T, MnO, CaO, Na_2O, K_2O, and P_2O_5. Smithsonian standards VG-2 glass, VG-A99 glass, VG-568 glass, Kakanui hornblende, magnetite, Durango apatite, scapolite, San Carlos and Stillwater olivine, and Johnstown hypersthene (Jarosewich et al., 1980) were used as standards.

4 Results

4.1. $Fe^{3+}/\sum Fe$ of the reference glasses

Of the sixteen basaltic glasses in our calibration, the Mössbauer spectra of the thirteen with >8% ferric iron were successfully fit with the 2D Gaussian model of Alberto et al. (1996) with two doublets, one with a low isomer shift corresponding to ferric iron and one with a high isomer shift corresponding to ferrous iron. These glasses span a range in $Fe^{3+}/\sum Fe$ of approximately 0.088 to 0.611 (Table 2). The quality of the fits for these glasses is characterized by reduced chi-squared values below 2. We show eight representative Mössbauer spectra and fits in Fig. 4 that span the full range of our calibration from QFM −3.5 to QFM +4.5.

Reasonable fits could not be obtained for the three most reduced glasses (AII_−35, AII_−25, and LW_−30). Transmission between the two broad bands that correspond to ferrous iron continues to decrease with falling fO_2 of equilibration for these three glasses (Figure A2), even over this very narrow fO_2 range, reflecting an ever smaller contribution from Fe^{3+} (Wilke et al., 2005). Nevertheless, the modeled $Fe^{3+}/\sum Fe$ is ~0.08 for all three reduced glasses with either one or two ferrous doublets. Difficulty resolving the ferric contribution below QFM-1 using Mössbauer has also been reported by other investigators (e.g. Dyar et al., 1987; Rossano et al., 1999; Berry et al., 2003a; Botcharnikov et al., 2005; Wilke et al., 2005). In response, Berry et al. (2003a) assumed an iron redox based on the stoichiometry of the expected reaction $FeO + 0.25O_2 \rightarrow FeO_{1.5}$, while Wilke et al. (2005) fit the observed spectra with six Fe^{2+} doublets. In our case, the inclusion of additional doublets did not statistically improve the model fit and so all spectra are fit with only one distribution each for the ferrous and ferric components. We thus report the ferric Fe contents of the three most reduced melts as below detection by Mössbauer, although a better term might be “unresolveable” by Mössbauer because decreasing contributions from ferric iron can be seen to increase the transmission between the ferrous doublets (Figure A2) and the centroids for these glasses continue to decrease in energy (Table 2).

The $Fe^{3+}/\sum Fe$ ratios for the basaltic glasses that are resolvable by Mössbauer are in very good agreement with the predicted $Fe^{3+}/\sum Fe$ ratios derived using the empirical formulation of Kress and Carmichael (1991), which was calibrated for basalts and based on wet-chemistry measurements (Fig. 5). While several studies have found agreement between redox determinations made by Mössbauer and wet chemistry (Mysen et al., 1985a,b; Dingwell, 1991), other studies suggest that Mössbauer spectroscopy systematically overestimates Fe^{3+} (Lange and Carmichael, 1989; Ottonello et al., 2001). Based on the comparison with Kress and Carmichael (1991), we see little evidence for a systematic offset here, except for the three most reduced glasses discussed above. The agreement between the model of Kress and Carmichael (1991) and

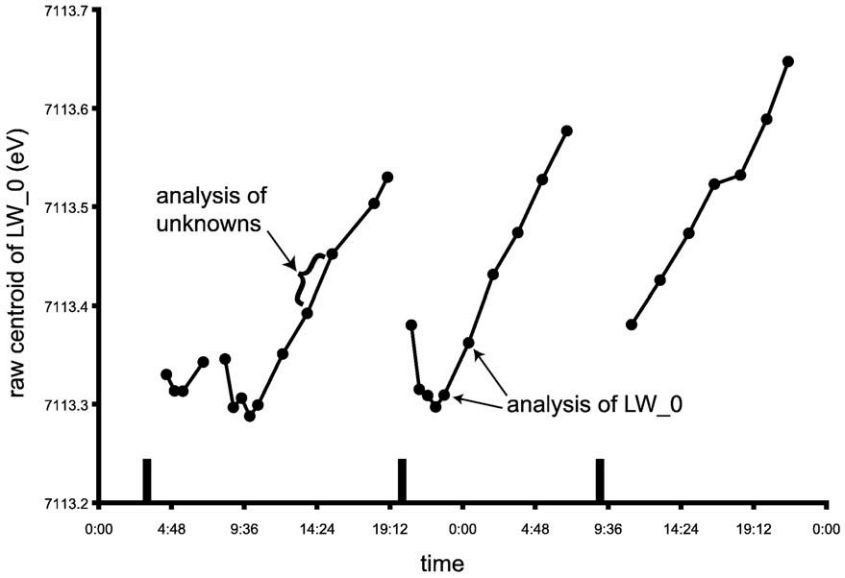

Fig. 3. The raw centroid energy of drift monitor LW_0 as a function of time over 24 h of analysis time at station X26A, NSLS, BNL. Ring reinjection is demarcated by vertical bars along the time axis. Drift in the early portions of each fill cycle is non-linear. After 2–2.5 h, the centroid drifts steadily upward in energy as the ring energy decays.

Table 2
Experimental conditions, average XANES centroid energy and intensity ratios, and $Fe^{3+}/\sum Fe$ measured by Mössbauer spectroscopy for glasses equilibrated at 1350 °C (except for 568_2, equilibrated at 1550 °C, and glasses from Moore et al., 1995).

Expt. #	log fO_2	ΔQFM	Single session drift-corrected centroid energy (eV)[a]	Cross session drift-corrected centroid energy (eV)[b]	Cross session[e] $I_{Fe^{3+}}/I_{Fe^{2+}}$	Cross session[e] $I_{Fe^{3+}}/[I_{Fe^{2+}}I_{Fe^{3+}}]$	$Fe^{3+}/\sum Fe$ predicted[c]	$Fe^{3+}/\sum Fe$ measured by Mössbauer	$\log(Fe^{3+}/Fe^{2+})$ Mössbauer
Basalts									
AII_−35	−10.19	−3.47	7112.074 (0.005)	7112.079 (0.009)	0.226 (0.012)	0.184 (0.008)	0.035	b.d	–
LW_−30	−9.86	−3.14	7112.079 (0.011)	7112.091 (0.011)	0.245 (0.019)	0.196 (0.012)	0.040	b.d	–
AII_−25	−9.31	−2.59	7112.098 (0.001)	7112.098 (0.006)	0.248 (0.008)	0.199 (0.005)	0.051	b.d	–
LW_−20	−8.72	−2.00	7112.108 (0.003)	7112.112 (0.003)	0.265 (0.007)	0.209 (0.005)	0.066	0.088 (0.0053)	−1.016
AII_−15	−8.22	−1.50	7112.138 (0.009)	7112.144 (0.010)	0.294 (0.010)	0.226 (0.006)	0.081	0.093 (0.0060)	−0.989
LW_−10	−7.72	−1.00	7112.156 (0.006)	7112.156 (0.002)	0.318 (0.014)	0.241 (0.008)	0.099	0.130 (0.0058)	−0.826
AII_−05	−7.20	−0.48	7112.211 (0.009)	7112.217 (0.011)	0.372 (0.018)	0.271 (0.010)	0.123	0.138 (0.0050)	−0.796
LW_0	−6.68	0.01	7112.299 (0.001)[d]	7112.299 (0.002)[d]	0.447 (0.013)	0.309 (0.006)	0.149	0.162 (0.0055)	−0.714
AII_0	−6.71	0.02	7112.276 (0.002)	7112.279 (0.006)	0.478 (0.033)	0.323 (0.017)	0.150	0.147 (0.0038)	−0.764
AII_05	−6.24	0.48	7112.366 (0.007)	7112.355 (0.011)	0.550 (0.019)	0.354 (0.008)	0.181	0.194 (0.0063)	−0.619
LW_10	−5.72	1.00	7112.438 (.001)	7112.439 (0.002)	0.666 (0.019)	0.400 (0.007)	0.211	0.235 (0.0053)	−0.513
AII_15	−5.24	1.48	7112.518 (0.010)	7112.511 (0.009)	0.780 (0.033)	0.438 (0.010)	0.257	0.247 (0.0044)	−0.484
LW_20	−4.73	2.00	7112.608 (0.005)	7112.611 (0.008)	0.934 (0.024)	0.483 (0.006)	0.295	0.303 (0.0140)	−0.362
AII_25	−4.25	2.47	7112.730 (0.010)	7112.740 (0.009)	1.243 (0.056)	0.554 (0.007)	0.350	0.356 (0.0038)	−0.257
AII_35	−3.22	3.50	7112.941 (0.003)	7112.937 (0.014)	1.822 (0.056)	0.645 (0.007)	0.462	0.484 (0.0040)	−0.028
AII_45	−2.20	4.52	7113.168 (0.004)	7113.163 (0.019)	3.060 (0.066)	0.754 (0.004)	0.575	0.611 (0.0026)	0.196
Rhyolites									
568_2	−3.09	1.93	7112.709 (0.010)	n.d.	0.985 (0.017)	0.496 (0.004)	n.d.	0.238 (0.0210)	−0.505
DT_46[f]	–	3.67	7113.244 (0.010)	n.d.	2.817 (0.132)	0.738 (0.009)	0.569[f]	0.600 (0.0146)	0.176
DT_39[f]	–	0.85	7112.858 (0.041)	n.d.	1.191 (0.085)	0.544 (0.018)	0.315[f]	0.320 (0.0250)	−0.327
H2O_63[f]	–	2.48	7113.298 (0.005)	n.d.	3.645 (0.100)	0.785 (0.005)	0.596[f]	n.d.	–
DT_29[f]	–	6.03	7113.454 (0.011)	n.d.	5.786 (0.327)	0.853 (0.007)	0.806[f]	n.d.	–
DT_31[f]	–	5.13	7113.282 (0.011)	n.d.	3.401 (0.222)	0.772 (0.013)	0.630[f]	n.d.	–
DT_18[f]	–	4.74	7113.355 (0.005)	n.d.	4.458 (0.116)	0.817 (0.004)	0.660[f]	n.d.	–

b.d. = below detection. n.d. = not determined.
[a] 1σ precision for repeated analyses, on separate areas of glass for a single beam session ($n=3$–4).
[b] 1σ precision for repeated analyses, on separate areas of glass across three beam sessions ($n=9$–12). Uncertainty in final significant digits should be read as 7113.192 ± 0.006 eV.
[c] Kress and Carmichael (1991).
[d] When LW_0 is analyzed as an unknown. Otherwise LW_0 ≡ 7112.3.
[e] $n=9$–12 except for rhyolites for which the values represent single session averages and precisions ($n=3$).
[f] $Fe^{3+}/\sum Fe$ determined by wet chemistry in the study of Moore et al. (1995).

Mössbauer above QFM-1 implies that the $Fe^{3+}/\sum Fe$ ratios predicted by Kress and Carmichael (1991) (3.5–5.0% ferric iron) may be accurate for the three experiments at the lowest fO_2; however, because we could not conclusively verify the $Fe^{3+}/\sum Fe$ of these most reduced glasses via an independent analytical methodology, we do not include them in our calibration. Ultimately, the calibration is not very sensitive to the inclusion or exclusion of these three glasses.

Mössbauer spectra were also acquired on three of the rhyolites: VG568_2, the natural obsidian equilibrated at high temperature in this study, and DT-46 and DT-39, the only glasses from Moore et al. (1995) with sufficient material to perform Mössbauer analyses. Mössbauer analysis of DT-46 and DT-39 yielded $Fe^{3+}/\sum Fe = 0.60\pm0.015$ and 0.32 ± 0.02, respectively (the 1σ error is much higher for the rhyolites than for the basalt glasses due to lower Fe concentrations and smaller sample quantities), which are in excellent agreement with the wet-chemistry values of 0.57 ± 0.06 and 0.31 ± 0.08 reported by Moore et al. (1995). These results are consistent with other studies that have also found Mössbauer spectroscopy to have no systematic offset from wet-chemical determinations (Mysen et al., 1985a,b; Dingwell, 1991).

4.2. XANES spectra

4.2.1. Basalts

The oxidation state of Fe is reflected in the energy and intensity of numerous XANES spectral features, such as the energy of the main absorption edge, the intensity of the edge shoulder ($1s\rightarrow4$ s transition) and edge crest ($1s\rightarrow4p$ transition), as well as several attributes of the pre-edge, including the area-weighted energy of the centroid and the ratio of pre-edge peak intensities (e.g., Berry et al., 2003a; Wilke et al., 2005). The smooth variation of these features with oxidation state can be seen, for example, in the full XANES spectra and pre-edges of the AII glasses investigated here (Fig. 6).

Baseline-subtracted pre-edge spectra for all basaltic glasses in this study are shown in Fig. 7. The centroid position can be seen to smoothly shift upwards in energy by approximately 1 eV as oxidation state shifts from ~3.5 to 60% ferric iron (corresponding to QFM −3.5 to QFM +4.5 for these basalts).

The shift of the centroid with $Fe^{3+}/\sum Fe$ and associated error bars are shown in Fig. 8 for centroid positions collected during three separate beam sessions. Note that both compositions, MORB and Hawaiite, were used to create the calibration curve, and any compositional dependence across this compositional range (Table 1) is thus encompassed by the associated uncertainties. Fitting each basalt composition independently, by any basis function, resulted in fits that were statistically indistinguishable. The centroids were reproducible from session to session with the same precision as within a single session (Section 4.2.2 and Table 2) due to the application of the drift monitor. These data are best modeled with a second-order polynomial with $R^2>0.999$ (Table 3). To translate this into a precision in $Fe^{3+}/\sum Fe$ for unknown samples, we report a full propagation of the errors in Section 4.2.2.

4.2.2. Precision of basalt calibration based on centroid energy

Deconvolution of the fluorescence Fe K pre-edge centroid coupled with correction for energy drift provides a robust measure of oxidation state regardless of sample Fe content, thickness, and detector configuration over the range investigated here. The empirical drift-corrected precision (1σ) of the area-weighted centroid positions within a single beam session ($n=3$–6 spots) is 0.008 ± 0.005 eV for all glasses (i.e., not the precision of a single Gaussian peak, rather the precision of the area-weighted average energy — the centroid — of the

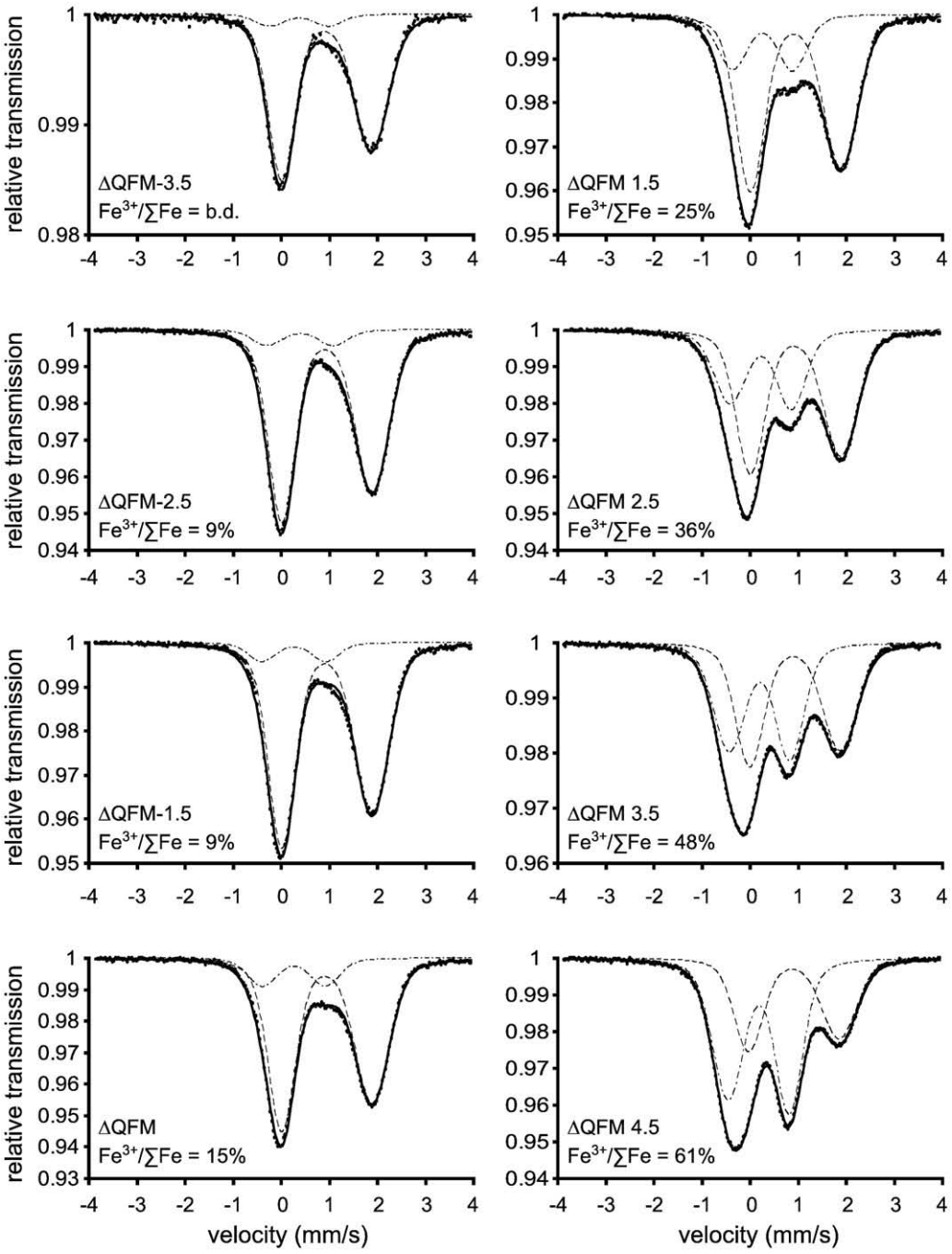

Fig. 4. Mössbauer spectra of eight representative basaltic reference glasses spanning the full range of fO_2 investigated (QFM −3.5 to +4.5). The dashed and dash–dot curves represent the contributions of Fe^{2+} and Fe^{3+}, respectively, to the Mössbauer spectrum. Dots represent the raw data and the solid black line represents the best fit to the data.

pre-edge feature). For a Gaussian model, the theoretical precision of the centroid is the energy step divided by the square root of the number of channels over which the Gaussian is fit ($0.1/\sqrt{80} = 0.01$), which compares favorably with the observed empirical precision. We show below that application of the drift monitor prevents degradation of the centroid precision from this theoretical value. With the Si (311) monochromator, the standard deviations of the centroid positions did not improve when stepping energy at increments smaller than 0.1 eV over the pre-edge peaks.

The practical application of the calibration shown in Fig. 8 is to the determination of $Fe^{3+}/\sum Fe$ in unknown basaltic glasses. Uncertainty in $Fe^{3+}/\sum Fe$ must take into account not only the reproducibility of individual reference glass centroids, but also the goodness-of-fit of the model function, the errors associated with the $Fe^{3+}/\sum Fe$ of the reference glasses determined by Mössbauer spectroscopy, and the session-to-session reproducibility of the calibration curve. The goal of our exercise, then, is to determine the true uncertainty in predicted values of $Fe^{3+}/\sum Fe$ for unknown glasses, based on measurements of centroid energy.

Uncertainties in centroid position and $Fe^{3+}/\sum Fe$ for the experimental reference glasses are central to propagating error through to analyses of unknowns. The overall empirical, drift-corrected, analytical precision (1σ) of centroid positions, by which we mean our ability to reproduce a measurement of the area-weighted pre-edge centroid energy across multiple beam sessions, is also 0.008 ± 0.005 eV — the same average precision with which we determine a centroid within a single beam session (Table 2). The Mössbauer uncertainties reported in Table 2 reflect the uncertainty in the Mössbauer spectral fits (the

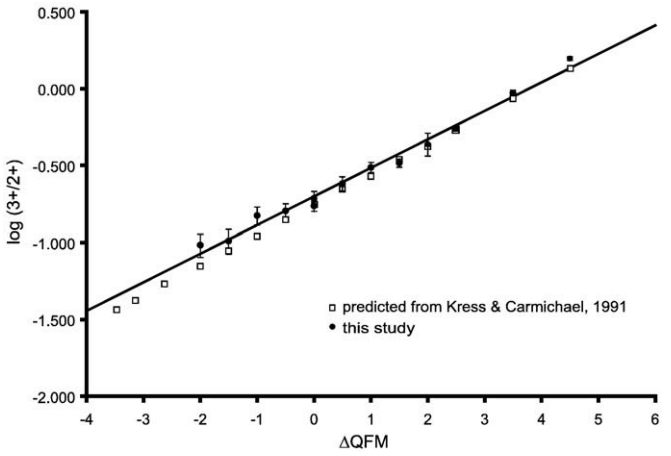

Fig. 5. Log (Fe^{3+}/Fe^{2+}) versus fO_2 relative to the QFM buffer for the 13 glasses for which Fe^{3+}/Fe^{2+} ratios could be determined by Mössbauer spectroscopy. Solid line is a weighted least-squares linear regression of the data. Also plotted are the predicted Fe^{3+}/Fe^{2+} ratios for these compositions at the experimental oxygen fugacities according to the empirical algorithm of Kress and Carmichael (1991).

scatter of the data around the model fit), and are typically on the order of ±1 to 6% $Fe^{3+}/\sum Fe$, consistent with other Mössbauer studies (Mysen et al., 1985a,b; Dyar et al., 1987).

To propagate these uncertainties through the calibration curve, we applied a weighted least-squares, second-order polynomial fit to the 13 most oxidized reference glasses shown in Fig. 8 (those for which we obtained good fits to the Mössbauer spectra), taking into account the uncertainties reported in Table 2. With these associated uncertainties, the unreduced chi-square goodness-of-fit statistic is equal to 45. This statistic should be on the order of 10 (the number of data points ($N=13$) minus the degrees of freedom in the fit ($M=3$)), indicating that either (1) a second-order polynomial model is not appropriate for the data, or (2) the uncertainty in $Fe^{3+}/\sum Fe$ is underestimated. There is no structure in the residuals between predicted $Fe^{3+}/\sum Fe$ and measured $Fe^{3+}/\sum Fe$ as a function of centroid position, indicating that a second-order polynomial is appropriate for these data, and we conclude that the errors in $Fe^{3+}/\sum Fe$ are underreported. Indeed, the actual uncertainties

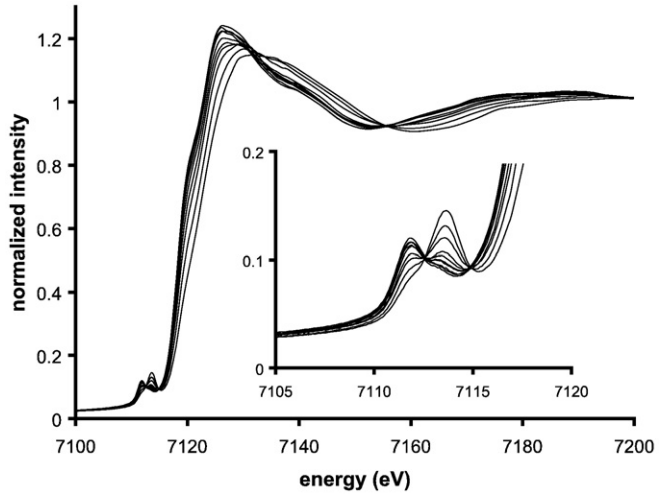

Fig. 6. Edge-step normalized XANES spectra, drift-corrected in energy, of the 10 "All" composition (MORB) basaltic glasses studied (LW glasses omitted for clarity) with $Fe^{3+}/\sum Fe$ ranging from <0.088 (i.e., including the most reduced glasses for which $Fe^{3+}/\sum Fe$ could not be resolved by Mössbauer spectroscopy) to 0.611. For this composition, the Fe oxidation states correspond to oxygen fugacities ranging from QFM −3.5 to QFM +4.5. Inset shows a magnified view of the pre-edge. The edge jump and edge crest move progressively higher in energy as a function of increasing $Fe^{3+}/\sum Fe$, and the contribution of the peaks corresponding to ferrous and ferric iron shifts smoothly as a function of $Fe^{3+}/\sum Fe$.

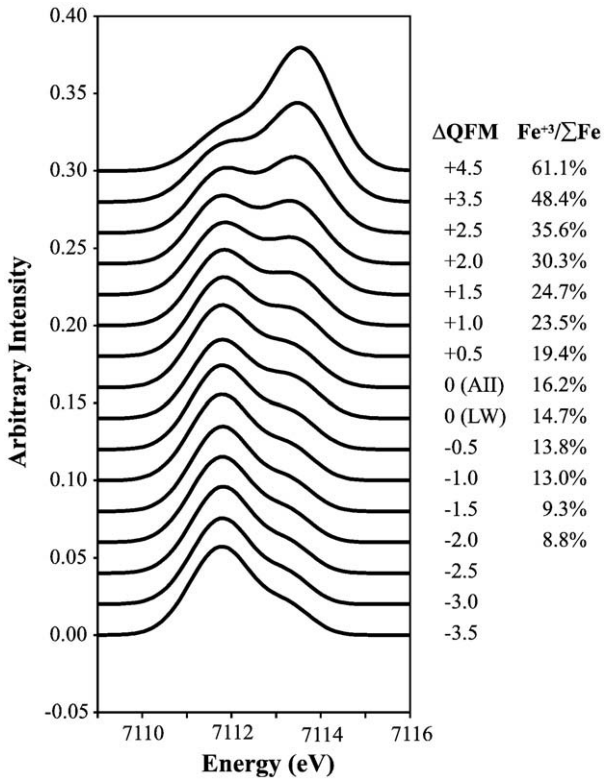

Fig. 7. The Fe 1s → 3d pre-edge transition, baseline-subtracted and drift-corrected, for all 16 basaltic reference glasses in this study. Spectra are vertically offset for clarity.

in $Fe^{3+}/\sum Fe$ determined by Mössbauer are probably much larger than indicated by the statistical scatter of the data around the model Lorentzians because it is unknown whether or not the fits reach a global minimum. To properly assign uncertainty in $Fe^{3+}/\sum Fe$ for this calibration then, we rescaled the uncertainty in $Fe^{3+}/\sum Fe$ for the reference glasses by $\sqrt{(\text{chisq}/(N-M))} = \sqrt{(45/10)} \sim 2.1$. The resultant uncertainties are displayed as the $Fe^{3+}/\sum Fe$ error bars in Fig. 8. We performed a second weighted least-squares fit to the data with the new

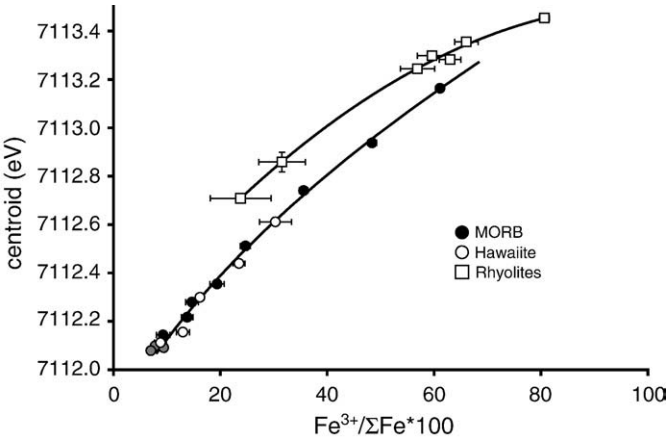

Fig. 8. Centroid energy versus $Fe^{3+}/\sum Fe*100$ for basalts (circles) and rhyolites (squares). Centroid positions for basalts were acquired in three separate sessions at X26A; the drift-corrected centroid values are indistinguishable from session to session. Error bars in $Fe^{3+}/\sum Fe$ are rescaled (enlarged) to achieve a reduced chi-squared of ~10 for the weighted second-order polynomial fits (see Section 4.2.2 for details). The error bars in centroid position equal the 1σ standard deviation of the average centroid position ($n=9$ per basalt sample; $n=3$ per rhyolite sample) and are smaller than the symbol size. The three gray points are the three most reduced basaltic glasses, for which satisfactory Mössbauer fits could not be obtained. These points were not included in the polynomial fit but are shown for reference.

Table 3
Regression coefficients from least-squares SVD fits with error estimates.

			Coefficients			1σ uncertainty			Average 1σ $Fe^{3+}/\sum Fe*100$
	x	μ	a	b	c	a	b	c	
Basalt	Centroid	7112.45876	22.99081	43.91273	14.68104	0.4075	1.3163	2.6737	0.45
	$IFe^{3+}/[IFe^{3+}+IFe^{2+}]$	0	2.66317	16.69170	80.96362	2.5188	11.4775	11.4023	0.52
	IFe^{3+}/IFe^{2+}	0	1.02469	34.67619	−4.91407	0.7983	1.4193	0.4067	0.45
Rhyolite	Centroid	7113.17147	50.17519	86.65910	72.29489	1.7320	5.0297	19.9389	1.89
	$IFe^{3+}/[IFe^{3+}+IFe^{2+}]$	0	94.37213	−299.67873	331.61669	67.7658	193.8462	135.9166	2.98
	IFe^{3+}/IFe^{2+}	0	13.14089	16.82717	−0.90087	9.4928	4.9395	0.5980	2.77

$Fe^{3+}/\sum Fe = a + b(x-\mu) + c(x-\mu)^2$ where x = measured quantity against which $Fe^{3+}/\sum Fe$ was regressed.

error estimates, and, by construction, the unreduced chi-square goodness-of-fit statistic is equal to ~10. The total uncertainty (1σ) in predicted $Fe^{3+}/\sum Fe$ derived from the calibration for unknown glasses, accounting for the full covariance structure of the fitted coefficients, is ±0.0045 (Table 3). The quoted precision is strictly valid for glasses with ≥8% ferric iron, because below that we are unable to independently validate the ferric iron contents of the reference glasses.

The precision with which $Fe^{3+}/\sum Fe$ could be determined from the centroid energy from the calibration of Wilke et al. (2005) for two undoped natural basalts of very similar composition is ±0.0288, versus 0.0045 here. We now explore the factors that influence the precision of the calibration in the present study. Four factors were evaluated for their contribution to the precision of the calibration: (1) monochromator resolution, (2) extraction of the centroid from curve fitting, (3) drift monitoring, and (4) the number of reference glasses in the calibration.

While Berry et al. (2003a) state that factors (1) and (2) "are not important for an accurate determination of oxidation state," we find that they do influence the precision. If we extend the above analysis to measurements made with a Si (111) monochromator (all other factors being equal) the precision with which the area-weighted centroid could be determined would degrade by a factor of twenty, to ±0.16 eV (from ±0.008 eV with a Si (311) monochromator). The corresponding loss in precision in $Fe^{3+}/\sum Fe$ would be a factor of ~3.5, to ±0.0158 (down from ±0.0045). Indeed, we believe this to be a primary factor influencing our precision and a reflection of the better accuracy that the higher resolution lattice cut provides in evaluating the relative areas of each multiplet peak in the pre-edge. The extraction of the centroid from the pre-edge feature variably affects the overall precision of the calibration, depending on the reproducibility of the fit. For example, if the model component functions are fit in sequence instead of simultaneously, if the energy range over which the pre-edge is fit is decreased, or if the Gaussian centers are not allowed to vary in energy, the precision of the centroid position can be degraded by up to a factor of 5. If the fit is equally poor for all glasses (reference glasses in the calibration and unknowns), then, in theory, the misfit should have no effect on the precision of the empirical calibration; however, this is rarely to be the case. We find, therefore, that the fitting routine matters insofar as that the quality of the fit is the same for all spectra across the range of pre-edge shapes. A very precise fit provides the best means of ensuring that reference glasses and unknowns are treated similarly. The choice of mathematical function (e.g. Gaussian vs. pseudo-Voigt) probably only matters to the extent that it achieves this end (Section 3.2.2).

The importance of monitoring instrumental drift will vary according to the nature of the light source and the beam line being used. At X26A we monitor variations in the incident photon flux (I_0), primarily due to current decay in the storage ring and drifts in incident monochromatic energy reflecting changes in thermal load on the monochromator with time. Cryo-cooled monochromators should display smaller thermal effects. At X26A the raw centroid position of glass LW_0 varies by 0.25–0.30 eV on average, with a standard deviation of 0.06 eV, which is >7x larger than our drift-corrected centroid precision. Using raw centroid values, instead of drift-corrected values, to calibrate yields a precision in $Fe^{3+}/\sum Fe$ of ±0.0068 (all other factors equal), or about 34% lower than with the drift correction in place, for a single beam session. This does not take into account the gains in reproducibility from session to session, which are even greater, as changes in collection conditions can easily move the reference energy by at least 0.2–0.3 eV.

Finally, the precision of any calibration depends on the number of reference points in the calibration. We base our precision on 13 reference glasses from 8.8 to 61% ferric iron. If only six reference glasses covered that range, it would reduce the precision in $Fe^{3+}/\sum Fe$ by about a factor of two, to ±0.0099.

4.2.3. Effects of self-absorption on pre-edge centroid intensities and energy

Self-absorption becomes a factor for fluorescence detection when the penetration depth into the sample is dominated by the absorbing atom, in this case iron. Self-absorption serves to attenuate the oscillatory structure of the XANES. For these reference glasses notable self-absorption effects were observed in the basalts (~8 at.% Fe) and the NCZ-4 rhyolite (~4.5 at.% Fe). Since our fitting procedure weights the calculated centroid energy based on the intensities of the pre-edge multiplets, we evaluated the potential effects of self-absorption on the calculated centroid energy. We find that spectra corrected for self-absorption using the FLUO algorithm developed by Daniel Haskel (University of Washington, USA) yield identical centroids to uncorrected spectra, indicating that the centroid position is insensitive to self-absorption (Botcharnikov et al., 2005). We verified this empirically for an expected range of sample thicknesses by preparing wafers of glass LW_0 at 30, 76, 100, and 300 μm thickness. All four samples returned the same centroid position to within 0.01 eV (within the precision of our analyses). The total integrated intensity of the pre-edge, however, increased after correction for self-absorption, as expected. A clear consequence of this effect is that, while self-absorption corrections do not significantly alter the centroid energy or the calculated $Fe^{3+}/\sum Fe$, an evaluation of differences in site geometry between samples with notable compositional differences requires very careful evaluation of self-absorption effects. If compositional heterogeneity exists at micrometer spatial resolution, this can pose a significant challenge.

It is also worthwhile to note that for materials with high and variable Fe concentrations measured in fluorescence, high detector dead times yield similar effects to those of self-absorption, changing the intensity of the pre-edge peak relative to the edge step. While detector dead time correction methodology is well-established, for array detectors it is expected that the differing elements will require individual pulse-pileup corrections that can be complex and variable between synchrotron beam sessions. This can lead to session-to-session variations in integrated pre-edge intensity on the same samples.

These effects therefore make it difficult to quantitatively compare Fe coordination geometry in the basalts and rhyolites, which have very different Fe concentrations (see also discussion by Botcharnikov et al. (2005)). Again, however, in our evaluations these effects have no notable affect on our calculated centroid energies within our quoted precision.

4.2.4. Determination of oxidation state using intensity ratios

Following Wilke et al. (2005), we also investigate the use of baseline-subtracted pre-edge intensity ratios (i.e., the ratio of the total area of the Fe^{3+} peak [$I(Fe^{3+})$] to the area of the Fe^{2+} peak [$I(Fe^{2+})$], or $I(Fe^{3+})/I(Fe^{2+})$) to quantify Fe oxidation state. Wilke et al. (2005) note that the limiting factor in their determination of oxidation state is the precision with which the centroid position can be determined (± 0.05 eV in their study). They conclude that, because intensity ratios vary over a wider range, they provide the most sensitive method for the determination of oxidation state, with the best correlation obtained by taking the ratio of $I(Fe^{3+})$ to the sum of intensities of both pre-edge peaks (i.e. $I(Fe^{3+})/[I(Fe^{3+})+I(Fe^{2+})]$).

In contrast to integrated pre-edge intensity, we find that intensity ratios are less sensitive to self-absorption and dead time. The relationship between either $I(Fe^{3+})/I(Fe^{2+})$ or $I(Fe^{3+})/[I(Fe^{3+})+I(Fe^{2+})]$ and $Fe^{3+}/\sum Fe$ can be modeled with a quadratic polynomial (Table 3, Fig. 9) and either can be used to determine the oxidation state of glasses. In addition, relative to centroids, intensity ratios are insensitive to energy drift, which is useful if a drift monitor is not employed.

When energy drift is accounted for, however, we find centroids to be more reproducible from session to session than intensity ratios, and that $Fe^{3+}/\sum Fe$ can be determined with greater precision using the centroid position. We also note that, above 50% ferric iron, intensity ratios display more scatter as a function of $Fe^{3+}/\sum Fe$ than centroids (Wilke et al. (2005), their figure 10), which becomes a factor here for the rhyolites. Finally, because pre-edge intensities are more sensitive than pre-edge energies to Fe coordination geometry (Wilke et al., 2005), they will also be more prone to errors arising from variations in Fe coordination (Berry et al., 2003a). This may particularly impact the application of this method to natural samples where variable quench rates may influence the coordination geometry of Fe (e.g., Dyar et al., 1987; Wilke et al., 2002; Metrich et al., 2006). For these reasons, we conclude that determination of the centroid is the most robust means of determining oxidation state, but that in cases where energy drift cannot be monitored, intensity ratios may be better employed.

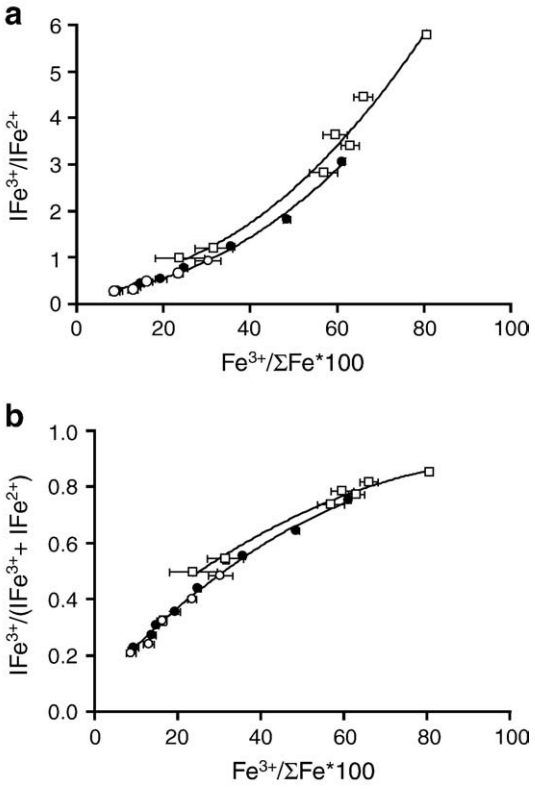

Fig. 9. The ratio of Gaussian component intensities (a) $I(Fe^{3+})/I(Fe^{2+})$ and (b) $I(Fe^{3+})/[I(Fe^{3+})+I(Fe^{2+})]$ as a function of $Fe^{3+}/\sum Fe*100$, after Wilke et al. (2005). Symbols are as in Fig. 8. Average values are plotted with 1σ error bars for $n=9$ (3 points/session × 3 beam sessions) for basalts and $n=3$ for rhyolites. In contrast to absolute values for integrated pre-edge intensity, the intensity ratios are not very sensitive to self-absorption or detector pulse-pileup, and in contrast to centroid position, intensity derived features are not very sensitive to energy drift.

4.2.5. Rhyolites

The pre-edge centroids of the sodium–silicate glasses from the study of Moore et al. (1995) and the natural Yellowstone rhyolite equilibrated at 1 atm in this study (568_2) also shift smoothly with $Fe^{3+}/\sum Fe$ (Fig. 8). The rhyolites from Moore et al. (1995) are peralkaline, whereas VG568_2 is metaluminous. These compositional variations do not appear to affect the relationship between the centroid and $Fe^{3+}/\sum Fe$ within the compositional range of the rhyolites (Table 1 and Section 5), but more a more thorough study of rhyolitic compositions is needed. A weighted least-squares fit of a second-order polynomial to the seven rhyolite reference glasses, taking into account the full covariance structure of the fitted coefficients, results in a 1σ precision in $Fe^{3+}/\sum Fe$ equal to ± 0.019 (Table 3). The precision with which $Fe^{3+}/\sum Fe$ can be determined for the rhyolites is considerably better using the centroid calibration than either of the calibrations based on intensity ratio (Table 3), but this may simply reflect the fact that the rhyolites extend to higher oxidation state where intensity ratios display more scatter (Wilke et al., 2005).

4.2.6. Effect of long-term beam excitement

Other microbeam methods of determining valence states of redox-sensitive elements (e.g., sulfur K-α energy shifts by electron microprobe) have well-known problems with beam excitation actively changing the oxidation state of the analyzed material (e.g., Rowe et al., 2007). This is particularly problematic with samples that have unbound water (e.g., soils and biological materials) and at higher photon fluxes such as those found at many third generation radiation sources (Ross et al., 2001; Tokunaga et al., 2003). To test the potential of long-term exposure to the μ-XANES X-ray beam for oxidizing/reducing Fe in our glasses, we analyzed reference glass LW_−20 ten times, including six analyses on fresh beam trajectories through the glass and four sequential analyses on a single spot (>60 min of continuous X-ray beam exposure). We observed no systematic shift in the centroid energy with continued beam excitation, after correction for well-constrained instrumental energy drift. The average drift-corrected centroid position for the six fresh spots was identical to that of the four sequential analyses within ± 0.001 eV. The standard deviations were also identical between the two sets of analyses and were equal to the precision quoted in the preceding section (± 0.01 eV). We therefore conclude that, within the limits of normal data acquisition, the X-ray beam has no damaging or oxidizing effect on Fe in the glasses.

5. Discussion

The aim of this contribution is to establish a calibration for the determination of $Fe^{3+}/\sum Fe$ in natural basalts by μ-XANES (e.g. Kelley and Cottrell, 2009). Here we address the applicability of the reference glasses to the study of natural basalts, which may vary in quench rate, water concentration, and bulk composition.

Wilke et al. (2002) demonstrated that quench rate, while having an effect on Fe coordination, has virtually no effect on Fe speciation in synthetic systems — a result in accord with wet-chemical and Mössbauer determinations (Dyar and Birnie, 1984; Dyar et al., 1987). Metrich et al. (2006) demonstrated an apparent temperature-

dependence of the centroid position during experiments where they recorded *in situ* XANES spectra on quartz-hosted silicic melt inclusions while varying the temperature. Pre-edge spectra showed an apparent increase in Fe^{3+} as temperature fell, even at a rate of 120 °C/s, concomitant with changing speciation of water in the inclusions. This novel study suggests that caution should be taken when applying XANES to naturally quenched glasses, such as sub-aerial lava flows and slowly cooled melt inclusions. Submarine basalt pillows, for example, exhibit cooling rates of 50–100 °C/s just 2–3 mm into the pillow; however, the glassy pillow rims likely cool at rates >400 °C/s (Xu and Zhang, 1999) and possibly >1000 °C/s (Zhou et al., 2000), making XANES an ideal tool to probe the iron redox of rapidly quenched submarine basalts. Application to rapidly quenched glassy melt inclusions in basalt tephra may also be possible, as long as care is taken to avoid samples that might have undergone reheating by subsequent eruptions (e.g., Burkhard, 2001).

The insensitivity of iron redox to quench rate (Dyar and Birnie, 1984; Dyar et al., 1987; Wilke et al., 2002) applies strictly to glasses where Fe is the only multi-valent element. An equally important finding is that trace elements such as Cr (Berry and O'Neill, 2004) and S (Metrich et al., 2009) do *not* retain their redox speciation through quench and become oxidized (while Fe becomes proportionally reduced) in compositions such as natural basalts, where multiple redox-sensitive species are found. While this has virtually no effect on Fe speciation due to its high abundance relative to S and Cr in most natural systems, it calls into question the ability to extract accurate oxidation state information from measurements of the S K-α edge (e.g. Carroll and Rutherford, 1988; Wallace and Carmichael, 1994; Rowe et al., 2006, 2007), which has widely been applied due to its high spatial resolution and accessibility with electron microprobe. These studies imply that the experimental reference glasses created for the present study are relevant for naturally quenched basalts, but also that redox "agreement" (or lack thereof) between Fe and S speciation in natural glasses is currently unknown.

By contrast, water does not appear to have an effect upon the speciation of Fe, as measured by XANES, in basaltic glasses, other than in how water affects system oxygen fugacity (Botcharnikov et al., 2005). This result is consistent with the wet-chemical studies of Gaillard et al. (2001) and Moore et al. (1995) and implies that the reference glasses created for calibration in this study are applicable for the extraction of $Fe^{3+}/\sum Fe$ ratios from both dry and hydrous basalts.

As discussed by Brown et al. (1995), alkali and alkaline earth element concentrations influence Fe coordination in silicate glasses, and this in turn could affect the centroid positions (Wilke et al., 2005). The two basalt compositions used here envelop a range of alkali and alkaline earth element concentrations (e.g., 0.15–1.5 wt.% K_2O, and 8.78–11.2 wt.% CaO), yet within this range, we see no resolvable effect of composition on the relationship between $Fe^{3+}/\sum Fe$ and centroid. In peralkaline melts, increasing K_2O concentration results in lower $Fe^{3+}/\sum Fe$ (Dickenson and Hess, 1981, 1986; Tangeman et al., 2001), but in non-peralkaline magmatic liquids, the reverse is seen (e.g., Dickenson and Hess, 1981, 1986; Kress and Carmichael, 1991). Both of these effects are related to the stabilization of tetrahedrally-coordinated Fe^{3+} with increasing alkali concentration. This could, in theory, affect the centroid position at a given ferric–ferrous ratio, due to coordination-induced changes in the pre-edge intensity. The redox shifts associated with increasing alkali concentration are negligible, however, in the context of most natural basaltic magmas. K_2O content might vary by up to 2 wt.% and the total K_2O content typically remains <2.5 wt.% in contrast to the experimental systems upon which these relationships are based, which contain 15–50 wt.% K_2O. In this study, we also see empirically that the effect of potassium on the relationship between $Fe^{3+}/\sum Fe$ and the centroid energy is unresolvable over the range of 0.15 to 1.5 wt.% K_2O.

As with potassium, we do not see a change in the relationship between the centroid and the $Fe^{3+}/\sum Fe$ ratio due to phosphorous, which, in contrast to K, stabilizes Fe^{2+} in silicate melts (Mysen, 1992; Toplis et al., 1994; Jayasuriya et al., 2004). This is consistent with Wilke et al. (2005), who did not observe any change in the centroid–$Fe^{3+}/\sum Fe$ relationship when comparing phosphorous-free basalts and those doped with up to 4.5 wt.% P_2O_5 (i.e., much higher than would be found in natural basalts).

In summary, our μ-XANES basalt calibration consists of two compositions, a mid-ocean ridge basalt (Shimizu et al., 1980) and a Hawaiite (Nichols and Rutherford, 2004). These two compositions span a range of major and minor element concentrations that encompass a diverse spectrum of basaltic magma types, including calc-alkaline basalts, thoeliites, high-potassium island arc basalts, and some alkali basalts. As discussed in Section 4.2.1, the relationship between the centroid and $Fe^{3+}/\sum Fe$ is independent of composition across this range and within the precision of this calibration. Independent polynomial fits to the two data sets were statistically indistinguishable. This suggests that we can determine the $Fe^{3+}/\sum Fe$ of basalts from diverse tectonic settings using this suite of reference glasses for calibration. The basalt calibration cannot, however, be applied to dramatically different compositions such as rhyolites.

To explore the versatility of the calibration, we prepared several rhyolitic glasses for XANES analysis as discussed in Section 2.1. It is clear from Fig. 8 and the uncertainties reported in Tables 2 and 3 that, at a given $Fe^{3+}/\sum Fe$, the rhyolite calibration curve is sub-parallel to the basalt curve, but offset to overall higher centroid energies. The average offset is only ~0.2 eV, but the displacement is easily resolvable given the precision of our analyses (Fig. 8). This shift likely reflects the influence of alkali and alkaline earth elements. As discussed above, the higher concentrations of network modifying cations in the rhyolite, such as potassium and sodium, should act to stabilize tetrahedrally-coordinated Fe^{3+}, thereby increasing the pre-edge intensity independent of the bulk $Fe^{3+}/\sum Fe$ ratio (Wilke et al., 2005; Metrich et al., 2006). It is difficult to quantitatively compare the coordination geometry in the rhyolitic and basaltic glasses in this study, however, because the integrated pre-edge intensity can also vary as a function of dead time and self-absorption when spectra are collected in fluorescence (Section 4.2.3).

By contrast, we have shown that the ratio of pre-edge peak intensities is not significantly affected by dead time, and it is clear that the pre-edge peak corresponding to Fe^{3+} is more intense for rhyolitic compositions than basaltic compositions at a given ratio of $Fe^{3+}/\sum Fe$ (Fig. 9). This contributes to the shift in centroid energy shown in Fig. 8. Moreover, we find that the drift-corrected Gaussian center positions at both low and high energy are consistently offset to higher energy in rhyolites relative to basalts at a given ratio of $Fe^{3+}/\sum Fe$ (by 0.03–0.1 eV and 0.01–0.15 eV, respectively). These factors both contribute to the offset of centroid energy to higher values in rhyolites relative to basalts. This observation is empirical and cannot be ascribed unambiguously to specific changes in the coordination geometry of Fe as discussed above, though undoubtedly differences in coordination must play a role in determining the energy position of the centroid (e.g., Wilke et al., 2001; Berry et al., 2003a; Farges et al., 2004; Wilke et al., 2005; Metrich et al., 2006).

Two previous studies have investigated the effect of major element composition on the relationship between the centroid and $Fe^{3+}/\sum Fe$. Within the precision of their measurements in transmission, Metrich et al. (2006) do not resolve a difference in the centroid vs. $Fe^{3+}/\sum Fe$ relationship for basalt and high-Si Pantellerite reference glasses, but they do see a difference in coordination environment, with basalts having a lower average coordination number (their figures 8 and 9). The discrepancy between finding a systematic shift in coordination environment on the one hand, but no corresponding shift in the centroid on the other, can be explained by the precision with which they report the centroid position (±0.1 eV) relative to intensity ratios, which have a greater dynamic range, and by the overall precision of their basalt calibration, which we calculate to be ±0.0185 $Fe^{3+}/\sum Fe$. Therefore, Metrich et al. (2006) would not necessarily have resolved an offset between their Si-rich Pantellerite and basalt if it were of the same magnitude as the offset we report here for rhyolite versus basalt.

Wilke et al. (2005), also working with spectra collected in transmission, compare natural Icelandic basalts to sodium–silicate glasses with 14–27 wt.% Na_2O. Even with this extreme compositional contrast, Wilke et al. (2005) report the centroids ($1\sigma \pm 0.05$ eV) for the sodium–silicate glasses as "shifted to slightly higher values" relative to the basalts at a given $Fe^{3+}/\sum Fe$. Though they report this shift as "within the uncertainty of the data," we note that their sodium–silicate glasses do fall outside of the 95% confidence interval for their fitted function, to higher centroid energies (their figure 9), consistent with our observations.

We now compare the relationship between the centroid energy and $Fe^{3+}/\sum Fe$ for a range of compositions from the literature (Fig. 10). The positions of the curves in absolute energy are not significant, depending only on the energy to which they are referenced (e.g., Fe foil), and therefore only the trends can be compared. The overall trend of increasing centroid with increasing $Fe^{3+}/\sum Fe$ is apparent across all compositions. Berry et al. (2003a) document a more linear trend for their An–Di eutectic composition than found by this study or Wilke et al. (2005) for basalts, though generally the trends found in all studies are remarkably consistent. Comparison of the scatter and error bars among the various studies reveals the benefits in precision afforded by the methodology presented here. These methodological improvements provide high enough resolution to clearly distinguish the effects of bulk composition on this general relationship, and to precisely and accurately resolve $Fe^{3+}/\sum Fe$ ratios in natural unknown glasses.

6. Conclusions

We present a methodology to determine $Fe^{3+}/\sum Fe$ in basaltic glasses with a precision of ± 0.0045 using the pre-edge centroid energy. The factors that most influence the precision include the use of a Si (311) monochromator, robust modeling of the pre-edge features, application of an energy drift monitor, and fO_2 resolution (i.e., number of reference glasses). The quoted precision can be achieved (i.e., analyses are reproducible) across multiple synchrotron beam sessions, even when spectral collection conditions (e.g., detector, sample geometry) change. A single reference glass, consistently applied as a drift monitor, can therefore yield the same precision in extracted $Fe^{3+}/\sum Fe$ as an entire complement of reference glasses if a robust calibration is initially achieved, thereby economizing time at future synchrotron sessions. This calibration for natural basalts encompasses a range of major and minor element concentrations appropriate for diverse basaltic magma types and, because data were collected in fluorescence, allows the $Fe^{3+}/\sum Fe$ to be determined for a wide range of geologically relevant samples varying in thickness and composition. The basalt calibration cannot be directly applied to dramatically different silicate compositions, such as rhyolites, for which the centroid shifts to higher energies (~0.2 eV) relative to basalt at a given $Fe^{3+}/\sum Fe$.

Acknowledgements

The authors gratefully acknowledge Tim Gooding's assistance with sample preparation, and Amelia Logan's assistance on the microprobe. We thank Shilpa Darivemula, Peter Cottrell, and David Kratzmann for their tireless shifts at X26A and Matt Newville for early discussions. Gordon Moore and Mac Rutherford are thanked for both samples and advice. We owe our deepest gratitude to Bjorn Mysen, whose generosity and scholarship made this work possible. The comments of two anonymous reviewers greatly improved the manuscript. Beamline X26A is supported by the Department of Energy (DOE) — Geosciences Division (DE-FG02-92ER14244 to the University of Chicago — CARS). Use of the NSLS was supported by DOE under contract no. DE-AC02-98CH10886. RF was supported by the Smithsonian Research Training Program (Bill & Jean Lane Foundation, Max Berry Donation) and the Carnegie Institution of Washington's REU program. We gratefully acknowledge support from Smithsonian's Scholarly Studies Program (to EC), a URI ADVANCE fellowship (to KK) and NSF awards EAR-0841108 (to KK) and EAR-0841006 (to EC).

Appendix A. Supplementary data

Supplementary data associated with this article can be found, in the online version, at doi:10.1016/j.chemgeo.2009.08.008.

References

Alberto, H.V., daCunha, J.L.P., Mysen, B.O., Gil, J.M., deCampos, N.A., 1996. Analysis of Mössbauer spectra of silicate glasses using a two-dimensional Gaussian distribution of hyperfine parameters. Journal of Non-Crystalline Solids 194 (1–2), 48–57.

Arculus, R.J., 1985. Oxidation status of the mantle — past and present. Annual Review of Earth and Planetary Sciences 13, 75–95.

Bajt, S., Sutton, S.R., Delaney, J.S., 1994. X-ray microprobe analysis of iron oxidation-states in silicates and oxides using X-ray-absorption near-edge structure (XANES). Geochimica Et Cosmochimica Acta 58 (23), 5209–5214.

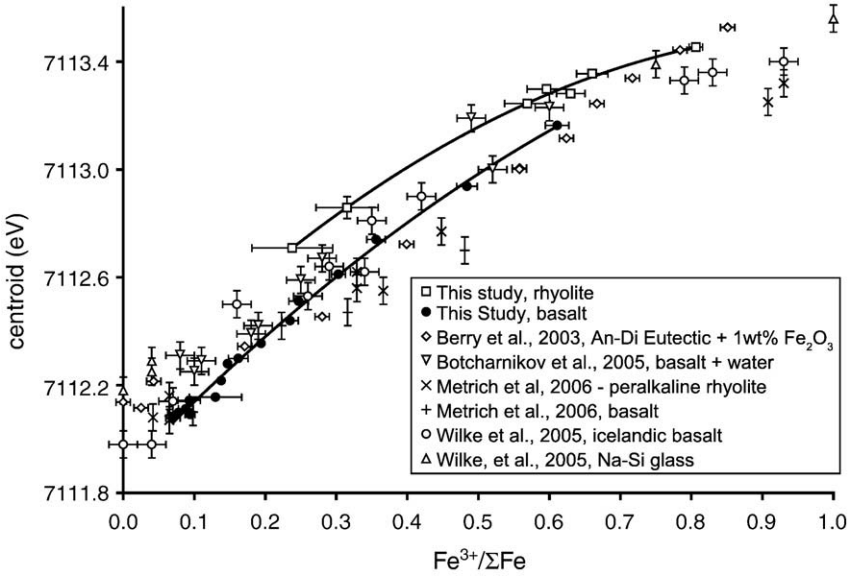

Fig. 10. $Fe^{3+}/\sum Fe$ versus centroid position from the literature for a range of compositions (Berry et al., 2003a; Botcharnikov et al., 2005; Wilke et al., 2005; Metrich et al., 2006). Error bars are as reported (if reported) by the authors of each study.

Berman, L.E. (1981). X-Ray Optics: An Extension to the DuMond Approach for Synchrotron Radiation. CHESS Technical Memo No. 24, Cornell University.
Berry, A.J., O'Neill, H.S.C., 2004. A XANES determination of the oxidation state of chromium in silicate glasses. American Mineralogist 89 (5–6), 790–798.
Berry, A.J., O'Neill, H.S., Jayasuriya, K.D., Campbell, S.J., Foran, G.J., 2003a. XANES calibrations for the oxidation state of iron in a silicate glass. American Mineralogist 88 (7), 967–977.
Berry, A.J., Shelley, J.M.G., Foran, G.J., O'Neill, H.S., Scott, D.R., 2003b. A furnace design for XANES spectroscopy of silicate melts under controlled oxygen fugacities and temperatures to 1773 K. Journal of Synchrotron Radiation 10, 332–336.
Berry, A.J., Danyushevsky, L.V., St, C., O'Neill, H., Newville, M., Sutton, S.R., 2008. Oxidation state of iron in komatiitic melt inclusions indicates hot Archaean mantle. Nature 455 (7215), 960–963.
Bezos, A., Humler, E., 2005. The Fe^{3+}/Σ Fe ratios of MORB glasses and their implications for mantle melting. Geochimica Et Cosmochimica Acta 69 (3), 711–725.
Bonnin-Mosbah, M., Simionovici, A.S., Metrich, N., Duraud, J.P., Massare, D., Dillmann, P., 2001. Iron oxidation states in silicate glass fragments and glass inclusions with a XANES micro-probe. Journal of Non-Crystalline Solids 288 (1–3), 103–113.
Botcharnikov, R.E., Koepke, J., Holtz, F., McCammon, C., Wilke, M., 2005. The effect of water activity on the oxidation and structural state of Fe in a ferro-basaltic melt. Geochimica et Cosmochimica Acta 69 (21), 5071–5085.
Brown, G.E., Farges, F., Calas, G., (Eds.), 1995. X-ray scattering and X-ray spectroscopy studies of silicate melts. Structure, Dynamics, and Properties of Silicate Melts, Reviews in Mineralogy.
Burkhard, D.J.M., 2001. Crystallization and oxidation of Kilauea basalt glass: processes during reheating experiments. Journal of Petrology 42 (3), 507–527.
Calas, G., Petiau, J., 1983. Coordination of iron in oxide glasses through high-resolution K-edge spectra — information from the pre-edge. Solid State Communications 48 (7), 625–629.
Carroll, M.R., Rutherford, M.J., 1988. Sulfur speciation in hydrous experimental glasses of varying oxidation-state — results from measured wavelength shifts of sulfur X-rays. American Mineralogist 73 (7–8), 845–849.
Cheatham, M.M., Sangrey, W.F., White, W.M., 1993. Sources of error in external calibration ICP-MS analysis of geological samples and an improved non-linear drift correction procedure. Spectrochimica Acta Part B: Atomic Spectroscopy 48 (3), 487–506.
Christie, D.M., Carmichael, I.S.E., Langmuir, C.H., 1986. Oxidation-states of midocean ridge basalt glasses. Earth and Planetary Science Letters 79 (3–4), 397–411.
Delaney, J.S., Dyar, M.D., Sutton, S.R., Bajt, S., 1998. Redox ratios with relevant resolution: solving an old problem by using the synchrotron microXANES probe. Geology 26 (2), 139–142.
Dickenson, M.P., Hess, P.C., 1981. Redox equilibria and the structural role of iron in alumino–silicate melts. Contributions to Mineralogy and Petrology 78 (3), 352–357.
Dickenson, M.P., Hess, P.C., 1986. The structural role and homogeneous redox equilibria of iron in peraluminous, metaluminous and peralkaline silicate melts. Contributions to Mineralogy and Petrology 92 (2), 207–217.
Dingwell, D.B., 1991. Redox viscometry of some Fe-bearing silicate melts. American Mineralogist 76 (9–10), 1560–1562.
Drager, G., Frahm, R., Materlik, G., Brummer, O., 1988. On the multipole character of the X-ray transitions in the pre-edge structure of Fe K-absorption spectra — an experimental-study. Physica Status Solidi. B, Basic Research 146 (1), 287–294.
Dyar, M.D., Birnie, D.P., 1984. Quench media effects on iron partitioning and ordering in a lunar glass. Journal of Non-Crystalline Solids 67 (1–3), 397–412.
Dyar, M.D., Naney, M.T., Swanson, S.E., 1987. Effects of quench methods on Fe^{3+}/Fe^{2+} ratios — a Mossbauer and wet-chemical study. American Mineralogist 72 (7–8), 792–800.
Dyar, M.D., Delaney, J.S., Sutton, S.R., Schaefer, M.W., 1998. Fe^{3+} distribution in oxidized olivine: a synchrotron micro-XANES study. American Mineralogist 83 (11–12), 1361–1365.
Dyar, M.D., Delaney, J.S., Sutton, S.R., 2001. Fe XANES spectra of iron-rich micas. European Journal of Mineralogy 13 (6), 1079–1098.
Farges, F., Lefrere, Y., Rossano, S., Berthereau, A., Calas, G., Brown, J.G.E., 2004. The effect of redox state on the local structural environment of iron in silicate glasses: a combined XAFS spectroscopy, molecular dynamics, and bond valence study. Journal of Non-Crystalline Solids 344 (3), 176–188.
Gaillard, F., Scaillet, B., Pichavant, M., Beny, J.L., 2001. The effect of water and fO_2 on the ferric–ferrous ratio of silicic melts. Chemical Geology 174 (1–3), 255–273.
Jackson, W.E., Deleon, J.M., Brown, G.E., Waychunas, G.A., Conradson, S.D., Combes, J.M., 1993. High-temperature XAS study of Fe_2SiO_4 liquid — reduced coordination of ferrous iron. Science 262 (5131), 229–233.
Jarosewich, E.J., Nelen, J.A., Norberg, J.A., 1980. Reference samples for electron microprobe analysis. Geostandards Newsletter—the Journal of Geostandards and Geoanalysis 4 (1).
Jayasuriya, K.D., O'Neill, H.S., Berry, A.J., Campbell, S.J., 2004. A Mossbauer study of the oxidation state of Fe in silicate melts. American Mineralogist 89 (11–12), 1597–1609.
Kavner, A., Walker, D., Sutton, S., Newville, M., 2007. Externally-driven charge transfer in silicates at high pressure and temperature: a XANES study. Earth and Planetary Science Letters 256 (3–4), 314–327.
Kelley, K.A., Cottrell, E., 2009. Water and the Oxidation State of Subduction Zone Magmas. Science 325 (5940), 605–607.
Kilinc, A., Carmichael, I.S.E., Rivers, M.L., Sack, R.O., 1983. The ferric–ferrous ratio of natural silicate liquids equilibrated in air. Contributions to Mineralogy and Petrology 83 (1–2), 136–140.
Kress, V.C., Carmichael, I.S.E., 1991. The compressibility of silicate liquids containing Fe_2O_3 and the effect of composition, temperature, oxygen fugacity and pressure on their redox states. Contributions to Mineralogy and Petrology 108, 82–92.
Lange, R.A., Carmichael, I.S.E., 1989. Ferric–ferrous equilibria in Na_2O–FeO–Fe_2O_3–SiO_2 melts — effects of analytical techniques on derived partial molar volumes. Geochimica et Cosmochimica Acta 53 (9), 2195–2204.
Lecuyer, C., Ricard, Y., 1999. Long-term fluxes and budget of ferric iron: implication for the redox states of the Earth's mantle and atmosphere. Earth and Planetary Science Letters 165 (2), 197–211.
Markwardt, C.B., 2008. Non-linear least squares fitting in IDL with MPFIT. Proc. Astronomical Data Analysis Software and Systems XVIII, Quebec, Canada. Astronomical Society of the Pacific, San Francisco.
McCanta, M.C., Dyar, M.D., Rutherford, M.J., Delaney, J.S., 2004. Iron partitioning between basaltic melts and clinopyroxene as a function of oxygen fugacity. American Mineralogist 89 (11–12), 1685–1693.
Metrich, N., Susini, J., Foy, E., Farges, F., Massare, D., Sylla, L., Lequien, S., Bonnin-Mosbah, M., 2006. Redox state of iron in peralkaline rhyolitic glass/melt: X-ray absorption microspectroscopy experiments at high temperature. Chemical Geology 231 (4), 350–363.
Metrich, N., Berry, A.J., O'Neill, H.S.C., Susini, J., 2009. The oxidation state of sulfur in synthetic and natural glasses determined by X-ray absorption spectroscopy. Geochimica et Cosmochimica Acta 73 (8), 2382–2399.
Moore, G., Righter, K., Carmichael, I.S.E., 1995. The effect of dissolved water on the oxidation-state of iron in natural silicate liquids. Contributions to Mineralogy and Petrology 120 (2), 170–179.
Mysen, B.O., 1992. Iron and phosphorus in calcium silicate quenched melts. Chemical Geology 98, 175–202.
Mysen, B.O., Richet, P., 2005. Silicate Glasses and Melts — Properties and Structure. Elsevier, New York.
Mysen, B.O., Shang, J., 2005. Evidence from olivine/melt element partitioning that nonbridging oxygen in silicate melts are not equivalent. Geochimica et Cosmochimica Acta 69 (11), 2861–2875.
Mysen, B.O., Carmichael, I.S.E., Virgo, D., 1985a. A comparison of iron redox ratios in silicate-glasses determined by wet-chemical and Fe-57 Mossbauer resonant absorption methods. Contributions to Mineralogy and Petrology 90 (2–3), 101–106.
Mysen, B.O., Virgo, D., Neumann, E.R., Seifert, F.A., 1985b. Redox equilibria and the structural states of ferric and ferrous iron in melts in the system CaO–MgO–Al_2O_3–SiO_2–Fe–O — relationships between redox equilibria, melt structure and liquidus phase-equilibria. American Mineralogist 70 (3–4), 317–331.
Nichols, M.G., Rutherford, M.J., 2004. Experimental constraints on magma ascent rate for the crater flat volcanic zone hawaiite. Geology 32 (6), 489–492.
Ottonello, G., Moretti, R., Marini, L., Zuccolini, M.V., 2001. Oxidation state of iron in silicate glasses and melts: a thermochemical model. Chemical Geology 174 (1–3), 157–179.
Roskoz, M., Toplis, M.J., Newville, M., Mysen, B.O., 2008. Quantification of the kinetics of iron oxidation in silicate melts using Raman spectroscopy and assessment of the role of oxygen diffusion. American Mineralogist 93, 1749–1759.
Ross, D.S., Hales, H.C., Shea-McCarthy, G.C., Lanzirotti, A., 2001. Sensitivity of soil manganese oxides: XANES spectroscopy may cause reduction. Soil Science Society of America Journal 65 (3), 744–752.
Rossano, S., Balan, E., Morin, G., Bauer, J.P., Calas, G., Brouder, C., 1999. Fe-57 Mössabuer spectroscopy of tektites. Physics and Chemistry of Minerals 26 (6), 530–538.
Rowe, M.C., Nielsen, R.L., Kent, A.J.R., 2006. Anomalously high Fe contents in rehomogenized olivine-hosted melt inclusions from oxidized magmas. American Mineralogist 91 (1), 82–91.
Rowe, M.C., Kent, A.J.R., Nielsen, R.L., 2007. Determination of sulfur speciation and oxidation state of olivine hosted melt inclusions. Chemical Geology 236 (3–4), 303–322.
Shimizu, N., Masuda, A. and Tadahide, U., (1980). Determination of Rare-Earth Elements in Leg 51, site 417 Samples. INIT REP DSDP 51–53: 1113–1120.
Tangeman, J.A., Lange, R., Forman, L., 2001. Ferric–ferrous equilibria in K_2O–FeO–Fe_2O_3–SiO_2 melts. Geochimica et Cosmochimica Acta 65 (11), 1809–1819.
Tokunaga, T.K., Wan, J.M., Firestone, M.K., Hazen, T.C., Olson, K.R., Herman, D.J., Sutton, S.R., Lanzirotti, A., 2003. In situ reduction of chromium(VI) in heavily contaminated soils through organic carbon amendment. Journal of Environmental Quality 32 (5), 1641–1649.
Toplis, M.J., Dingwell, D.B., Libourel, G., 1994. The effect of phosphorus on the iron redox ratio, viscosity, and density of an evolved ferro-basalt. Contributions to Mineralogy and Petrology 117 (3), 293–304.
Walker, D., Jurewicz, S., Watson, E.B., 1988. Adcumulus dunite growth in a laboratory thermal-gradient. Contributions to Mineralogy and Petrology 99 (3), 306–319.
Wallace, P.J., Carmichael, I.S.E., 1994. S-speciation in submarine basaltic glasses as determined by measurements of SK-alpha X-ray wavelength shifts. American Mineralogist 79 (1–2), 161–167.
Waychunas, G.A., Apted, M.J., Brown, G.E., 1983. X-ray K-edge absorption-spectra of Fe minerals and model compounds — near-edge structure. Physics and Chemistry of Minerals 10 (1), 1–9.
Waychunas, G.A., Brown, G.E., Ponader, C.W., Jackson, W.E., 1988. Evidence from X-ray absorption for network-forming Fe^{-2+} in molten alkali silicates. Nature 332 (6161), 251–253.
Wilke, M., Farges, F., Petit, P.-E., Brown Jr., G.E., Martin, F., 2001. Oxidation state and coordination of Fe in minerals: an Fe K-XANES spectroscopic study. American Mineralogist 86 (5–6), 714–730.
Wilke, M., Behrens, H., Burkhard, D.J.M., Rossano, S., 2002. The oxidation state of iron in silicic melt at 500 MPa water pressure. Chemical Geology 189 (1–2), 55–67.
Wilke, M., Partzsch, G.M., Bernhardt, R., Lattard, D., 2005. Determination of the iron oxidation state in basaltic glasses using XANES at the K-edge. Chemical Geology 220 (1–2), 143–161.
Wood, B.J., Bryndzia, L.T., Johnson, K.E., 1990. Mantle oxidation-state and its relationship to tectonic environment and fluid speciation. Science 248 (4953), 337–345.
Xu, Z., Zhang, Y., 1999. Quantification of quench rates in water, air, and liquid nitrogen. Goldschmidt Conference Abstracts.
Zhou, W., Van der Voo, R., Peacor, D.R., Zhang, Y., 2000. Variable Ti-content and grain size of titanomagnetite as a function of cooling rate in very young MORB. Earth and Planetary Science Letters 179 (1), 9–20.